Physical Chemistry Chemical Physics

ARTICLE

Thermodynamic stability of non-stoichiometric $SrFeO_{3-\delta}$: a hybrid DFT study

Received 00th November 2018,
Accepted 00th November 2018

DOI: 10.1039/x0xx00000x

www.rsc.org/

Eugene Heifets,[*a,†] Eugene A. Kotomin,[b,c] Alexander Bagaturyants,[a,d] and Joachim Maier[b]

$SrFeO_{3-\delta}$ is mixed ionic-electronic conductor with complex magnetic structure which reveals also colossal magnetoresistance effect. This material and its solid solutions are attractive for various spintronic, catalytic and electrochemical applications, including cathodes for solid oxide fuel cells and permeation membranes. Its properties strongly depend on oxygen non-stoichiometry. *Ab initio* hybrid functional approach was applied here for a study of thermodynamic stability of a series of $SrFeO_{3-\delta}$ compositions with several non-stoichiometries δ, ranging from 0 to 0.5 ($SrFeO_3$ - $SrFeO_{2.875}$ - $SrFeO_{2.75}$ - $SrFeO_{2.5}$) as the function of temperature and oxygen pressure. The results obtained by considering Fe as all-electron atom and within the effective core potential technique are compared. Based on our calculations, the phase diagrams were constructed allowing the determination of environmental conditions for the existence of stable phases. It is shown that (within an employed model) only the $SrFeO_{2.5}$ phase appears to be stable. The stability region for this phase is re-drawn at the contour map of oxygen chemical potential, presented as a function of temperature and oxygen partial pressure. A similar analysis is also performed using experimental Gibbs energies of perovskite formation from the elements. The present modelling strongly suggests a considerable attraction between neutral oxygen vacancies. These vacancies are created during a series of above mentioned $SrFeO_{3-\delta}$ mutual transformations accompanied by oxygen release.

1. Introduction

Many cathode materials for solid oxide and protonic ceramic fuel cells (SOFC, PCFC) and oxygen permeation membranes are perovskite solid solutions with the general formula $(A_{1-x}Sr_x)(Fe_{1-y}B_y)O_{3-\delta}$, where A stands for Ba^{2+}, La^{3+}, Bi^{3+} or similarly large cations.[1-4] Strontium ferrate $SrFeO_{3-\delta}$ (SFO) is one of the parent materials for such solid solutions, and its study is a necessary step in the investigation of properties of complex cathode materials. SFO is a mixed ionic-electronic conductor (MIEC), used in many applications, such as SOFC cathodes,[5] gas sensing electrodes,[6] gas separation membranes[7] and photocathodes.[8] The composition of this material strongly depends on the temperature and oxygen partial pressure. Special measures, such as employing high oxygen pressure, are necessary to enforce a rather complete filling of crystalline sites with oxygen atoms (δ≈0)[9]. Four distinct phases of SFO were found[10,11] in air at temperatures up to 1400°C: cubic perovskite (space group (SG) $Pm\bar{3}m$, # 221, Fig. 1), tetragonal (SG $I4/mmm$, # 139, Fig. 2), orthorhombic (SG $Cmmm$, # 65, Fig. 3), brownmillerite (SGs $Imma$, #74, $Ibm2$, # 46, $Pbma$, # 57, $Pnma$, # 62, Fig. 2). These phases correspond to oxygen contents for the non-stoichiometries δ≈0 ($SrFeO_3$), δ≈0.125 ($SrFeO_{2.875}$), δ≈0.25 ($SrFeO_{2.75}$), δ≈0.5 ($SrFeO_{2.5}$), respectively. The first two phases are metallic, with a helical magnetic order at zero magnetic field, whereas the two latter phases are insulating with anti-ferromagnetic (AFM) spin ordering.

The AFM spin ordering in $SrFeO_{2.75}$ exists among Fe^{3+} ions located within square pyramids, whereas spins on Fe^{4+} ions in octahedral surrounding are frustrated or disordered.[12] Direction of spins in $SrFeO_{2.5}$ changes from one cell to nearest one along all three lattice [100] directions (G-type AFM).[9] The

[a] Photochemistry Center, Federal Research Center "Crystallography and Photonics," Russian Academy of Sciences, Novatorov 7a, Moscow, 119421 Russia.
[b] Max Planck Institute for Solid State Research, Heisenbergstr. 1, Stuttgart 70569, Germany.
[c] Institute for Solid State Physics, University of Latvia, 8 Kengaraga str., Riga, LV-1586, Latvia.
[d] National Research Nuclear University MEPhI (Moscow Engineering Physics Institute), Kashirskoye sh. 31, Moscow, 115409 Russia.
† Email: eheif5719@sbcglobal.net

Electronic Supplementary Information (ESI) available: phase diagrams for $SrFeO_3$, $SrFeO_{2.875}$ and $SrFeO_{2.75}$. See DOI: 10.1039/x0xx00000x

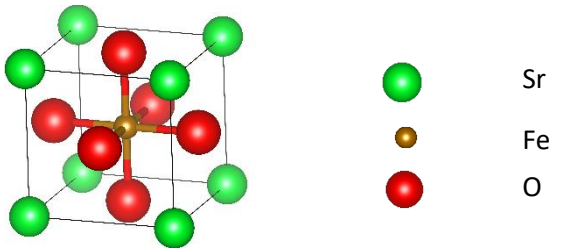

Fig. 1 Structure of $SrFeO_3$. This figure as well as crystal structures presented in following Figs. 2 - 5 are prepared using Vesta code.[13]

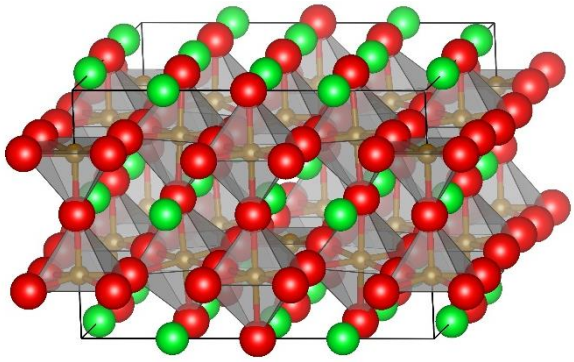

Fig. 2 Structure of $SrFeO_{2.875}$.

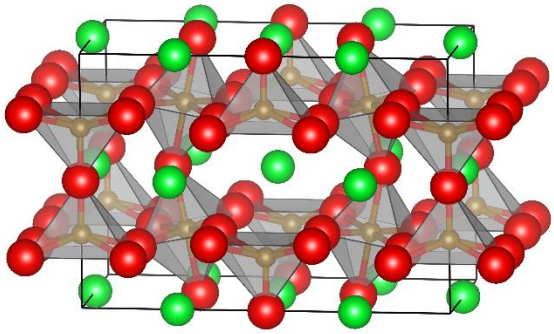

Fig. 3 Structure of $SrFeO_{2.75}$.

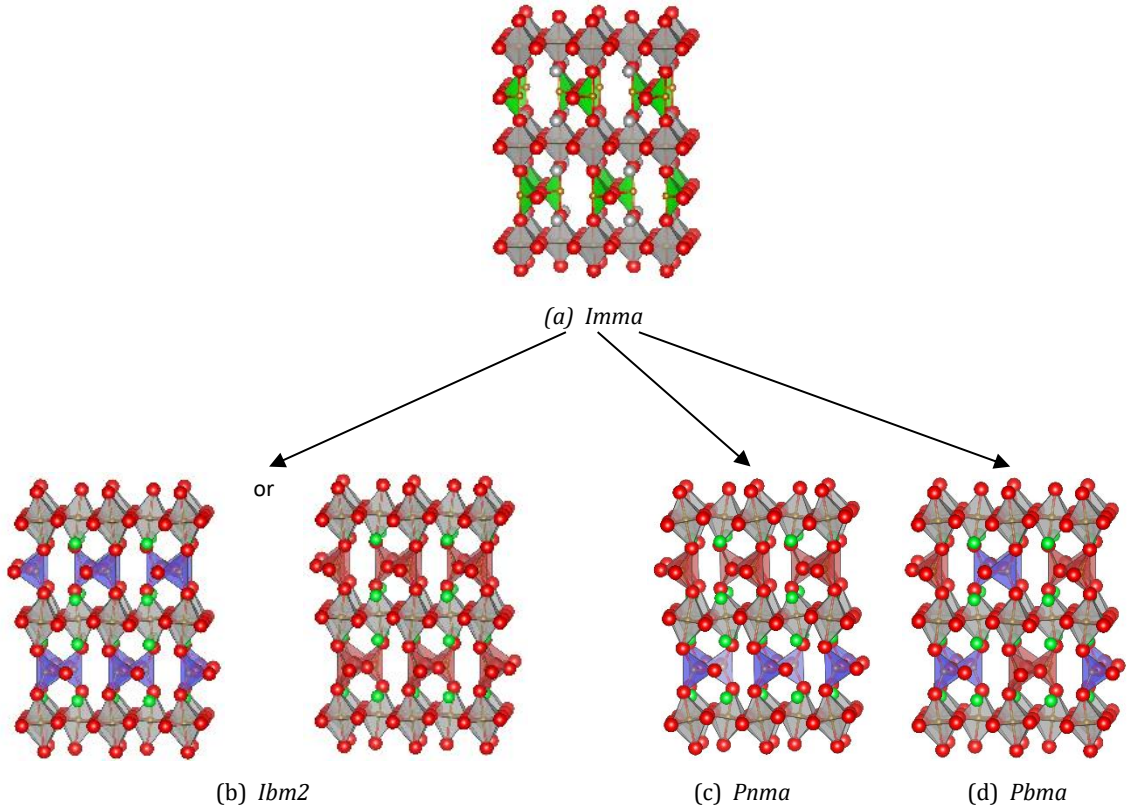

Fig. 4 Structures of four phases for $SrFeO_{2.5}$

Physical Chemistry Chemical Physics

ARTICLE

interest in SFO is also due to multiple magnetic phases causing colossal magnetoresistance effect, and due to the sensitive dependence of the magnetic properties on oxygen content.[14-16]

Understanding thermodynamic stability and the phase diagram of pure $SrFeO_{3-\delta}$ provides the basis for investigations of intrinsic defects (O vacancies), magnetic properties, surface structures, surface chemical reactions (e.g. oxygen reduction reaction), dependence of the properties on temperature, on oxygen content, and on the specific crystalline structure. Knowledge of the SFO phase diagram is vital for studies of solid solution formation, such as for above-mentioned SOFCs cathode materials, their possible crystalline structures, structural stability and other properties. The chemical phase diagram also provides a valuable guidance for synthesizing these materials.

In the present study, we are interested in changes occurring in SFO on variation of temperature and oxygen non-stoichiometry. Therefore, we restrict ourselves only to those SFO phases, which contain equal amounts of Sr and Fe atoms. Phase diagrams, describing areas of stability for different materials are characterized by the Gibbs energies of formation of these materials. Experimental data on energies of formation are available only for $SrFeO_{2.5}$.[17,18] The enthalpy of $SrFeO_{2.5}$ formation from binary oxides – strontium (SrO) and iron (Fe_2O_3) – was measured by high-temperature drop solution calorimetry in molten $2PbO{\cdot}B_2O_3$,[17] while the Gibbs energy of formation for several $Sr_nFe_mO_{n+3m/2}$ compounds, including $SrFeO_{2.5}$ were estimated in ref. 17 by electrochemical techniques using CaF_2 as electrolyte. To our best knowledge, no theoretical studies of SFO phase diagram exist so far, the recent modelling of all four above mentioned SFO phases[19] at 0 K is the closest to such an investigation. The authors of that study[19] considered the crystalline structures of four SFO phases and formation of single O vacancies therein. This modelling was performed using plane-wave basis set and the spin-polarized generalized gradient approximation (GGA), with the Perdew, Burke, and Ernzerhof (PBE) functional[19] employed to describe the exchange-correlation potentials. On-site Coulomb interaction in Fe ions was corrected using the Hubbard U parameter[21] to account for a strong electron correlation effects (DFT+U method).

In this study, we used the hybrid density functional (hDF) with local atom-centered basis sets to calculate the total energies for all involved materials, in continuation of our previous work,[22,23] on $LaFeO_3$ and $BiFeO_3$. Application of the same method allowed us to use the results of calculations for iron oxides obtained in these calculations. In the hDF method, the exchange part of employed density functional is mixed with a precise non-local Fock exchange term. The basis sets needed for our present modellings were also already optimized in the previous studies.[22,23] The use of hDF has the advantage of treating all cations and anions on the same ground, in contrary to commonly employed DFT+U approach, where the Hubbard correction U is applied only at d- or f-atomic orbitals. This allows us to avoid the ambiguity of employing the same value of the Hubbard U correction to atoms with different oxidation states and in different chemical surroundings. Also, the bond energy of the O_2 molecule calculated with the hDFs methods is in a very good agreement with its experimental value eliminating the need for their correction known for the GGA-type approach.[22-25]

In constructing phase diagrams, we followed the thermodynamic approach, in which the required energies of formation for various materials were calculated using the total energies obtained from quantum-mechanical electronic structure calculations. Such an approach was applied recently, for example, to $LaMnO_3$ [26] and used by us for investigations of $BiFeO_3$, [22] $LaFeO_3$,[23] $SrTiO_3$.[25]

Necessary details of the applied technique are described in Section 2. This section contains two subsections. The first one deals with specifics of the electronic structure computations for all considered crystal structures. The second subsection describes thermodynamic considerations necessary to build phase diagrams. The results of modelling are discussed in Section 3, where obtained crystal structures are described, and thermodynamic analysis of stability for all structures is presented. Finally, summary of the obtained results and conclusions are given in Section 4.

2. Theoretical

Computational details

Computations of the electron structure, optimization of crystalline structure and calculations of the total energies for considered SFO phases were performed using the CRYSTAL09 computer code[27] and the same computational parameters, to keep consistence with our previous similar modelling.[22,23] This code allows us to perform ab initio calculations of the electron structure of molecules and periodical multi-atomic structures, including crystals, by means of the Hartree-Fock method and by a number of various DFT and hDF techniques. The calculations employ the localized atomic (Gaussian-type) basis functions centered at atomic nuclei[28-30] and used to expand one-electron orbitals (linear combination of atomic orbitals - LCAO). The present simulations were performed using the hybrid B3PW functional,[31] which includes a mixture of the

nonlocal exact Fock's exchange, GGA,[31-34] and local density approximation (LDA)[35] exchange potentials, combined with the GGA correlation potential of Perdew and Wang.[34,36] Due to the presence of iron ions in the considered materials, one can expect considerable electron correlation effects. The use of a hDF in modelling Fe-containing materials considerably reduces self-interaction errors of the standard density functionals. As mentioned above, employing hDF also allows us to avoid corrections to compensate for overestimate in the bond energies of O_2 molecules[3,37] used as the reference state in the thermodynamic calculations.

The Monkhorst–Pack grids for integration over the Brillouin zone[29] in the reciprocal space have to be chosen in such a way, that the results of calculations for various materials with different unit cells were comparable. Therefore, the k-grids were chosen, to ensure that distances between neighboring points of the net are approximately the same for all materials. It is reasonable to take the calculations of $SrFeO_3$ as a reference for all other crystals. In the present study, we used an extended 2×2×2 $SrFeO_3$ cubic unit cell of 40 atoms, because it allows us to compare all possible magnetic orderings of this perovskite material (FM, AFM:A, AFM:C, and AFM:G). The computations employed the 8×8×8 Monkhorst–Pack grid. This size of the grid is sufficient to ensure convergence of the total energy for the employed extended unit cell. Modelling for $SrFeO_{2.875}$ and for $SrFeO_{2.75}$ employed the conventional unit cells (Fig. 2 and 3), which are twice as large as their primitive unit cells containing 78 and 38 atoms, respectively. Corresponding Monkhorst–Pack grids were chosen as 6×6×8 and 6×12×8, respectively. Computations for $SrFeO_{2.5}$ were also performed using conventional unit cells for all four possible phases. For phases with crystal symmetries $Imma$, $Ibm2$, $Pnma$ such unit cells contain 36 atoms (Fig. 4a-c) and 12x4x12 Monkhorst–Pack grids were used. The $SrFeO_{2.5}$ phase with $Pbma$ symmetry has twice a larger unit cell with 72 atoms (Fig. 4d) and the Monkhorst–Pack grid of size 8x4x12 was employed.

The inner core electrons of heavy atoms were replaced by the effective core potentials (ECPs) what allows us to reduce considerably computational time. The ECPs reproduce interactions of the replaced core electrons with the rest of electrons in the system. For a better description of atoms, electrons of two external (valence and core-valence) electron shells were not included into the ECPs but described explicitly. The scalar-relativistic energy-consistent ECPs developed by the Stuttgart/Cologne group[38] were used. Basis sets required for present simulations were optimized and published in our previous paper[23] and could be also found on the CRYSTAL code's web-site.[39] The ECP28MDF potential[40,41] and basis set contracted according to s411p411d11 pattern[42] were used for Sr atoms. Since O atoms have only two electron shells, all electrons at O atoms were described explicitly and an all-electron basis set[43] was applied. Computational time saving due to use of ECPs at Fe atoms is moderate because only 10 electrons occupy two inner core electron shells. Therefore, before starting massive use of ECP and respective basis set in the calculations, one has to evaluate and weight computer time savings versus loss of accuracy due to the ECP use. We performed modelling for both cases: (i) employing ECP10MFD potential[44,45] with respective basis set contracted according s411p411d411 scheme from[46] on Fe atoms, and (ii) all-electron Fe ion treatment with basis set from[47] contracted according s86411p6411d411 pattern, in order to make a choice for future modelling.

At ambient temperatures, spins of Fe atoms in various SFO phases have different magnetic orderings. There are three possible AFM phases in the perfect perovskite lattices (i) in the A-type AFM ordering the Fe ion spins are arranged ferromagnetically (parallel) within the (001) planes, but spins in the nearest neighbouring planes change orientation to opposite, (ii) in the C-type AFM spins are arranged ferromagnetically (FM) along one of the [001] directions, but have opposite (anti-parallel) arrangement in the planes perpendicular to this direction, and (iii) in the G-type AFM case spins on all nearest neighbour iron ions are oppositely directed. In the present simulations, all three SFO-AFM orderings were considered with different oxygen contents. However, in three phases ($SrFeO_{2.875}$, $SrFeO_{2.75}$, $SrFeO_{2.5}$) there is the lattice direction, which is characteristic for arrangement of layers in their crystal structures: 'c' ([001]) for $SrFeO_{2.875}$ and 'b' ([010]) for $SrFeO_{2.75}$ and $SrFeO_{2.5}$. Unit cells for these compounds shown in Figs. 2-4 are rotated, to align them with the Oz axis. In our calculations for the A and C types of AFM orderings, we limited ourselves to these arrangements.

The magnetic structure of SrFeO3 and SrFeO2.875 is known to be helical.[9] Such structure cannot be reproduced using the CRYSTAL code, because of its limitation to the collinear spin structures. Therefore, helical structures were replaced by ferromagnetic ones, which are close to these incommensurate helical magnetic structures.

Thermodynamic investigation of materials stability

The standard way to evaluate relative stabilities of different phases is to compare their Gibbs energies: the most stable material has the lowest Gibbs energies among its competitors. Because unit cells of crystals are small and their volume changes with temperature very little, the contribution of the *pV* term to Gibbs energies usually is neglected. According to,[48] the vibrational contributions to the internal energy and to entropy usually almost cancel each other. Thus, we neglect here the vibrational contributions without any significant effect on the phase diagram. Such an approximation allows us to replace the Gibbs energy (per formula unit) $G_{A_aB_bO_c}$ for a double oxide $A_aB_bO_c$ by the total electronic energy, obtained in the electronic structure calculations: $G_{A_aB_bO_c} \approx E_{A_aB_bO_c}$. Usually, atomic chemical potentials for each element are measured as deviations with respect to its standard state. For metals M=A or B, which standard state is a solid, this gives:

$$\Delta\mu_M = \mu_M - G_M^{bulk} \approx \mu_M - E_M \,, \qquad (1)$$

where G_M^{bulk} and E_M are Gibbs energy and the total energy (both are given per atom) in a metal M. The standard state for oxygen is O_2 gas. Therefore, the O atom chemical potential is

defined here as its deviation from the energy of an atom in O_2 molecule:

$$\Delta\mu_O(T, p_{O_2}) = \mu_O(T, p_{O_2}) - \frac{1}{2}E_{O_2}, \quad (2)$$

and the ideal gas model is employed to describe oxygen gas[48]:

$$\Delta\mu_O(T, p_{O_2}) = \frac{1}{2}\{\Delta G_{O_2}^{gas}(T, p^0) + k_B T ln(\frac{p_{O_2}}{p^0})\} + \delta\mu_O^0. \quad (3)$$

Here T is temperature in the system; p_{O_2} is oxygen gas partial pressure; $p_0 = 1$ atm. is the standard pressure; k_B is Boltzmann constant; the first term in brackets is the temperature change of the oxygen Gibbs energy at the standard pressure, and the correction $\delta\mu_O^0$ is used to match zeros for the experimental variation of the O chemical potential and for our theoretical estimates. The variation of the Gibbs energy for oxygen gas at standard pressure $\Delta G_{O_2}^{gas}(T, p^0)$ as a function of temperature was taken from experimental data collected in NIST Chemistry WebBook.[49]

While a material with a formula $A_aB_bO_c$ is stable, the chemical potentials of three elements involved are connected by the relation

$$a\Delta\mu_A + b\Delta\mu_B + c\Delta\mu_O \approx \Delta E_{f,A_aB_bO_c} \quad , \quad (4)$$

where the *energies of formation* ΔE_f for a compound $A_aB_bO_c$ (any of stoichiometric coefficients *a* or *b* could be equal to 0, to include into consideration also simple oxides) from elements are

$$\Delta E_{f,A_aB_bO_c} = E_{A_aB_bO_c} - aE_A - bE_B - \frac{c}{2}E_{O_2}. \quad (5)$$

According to Eq. (4), only two of three chemical potentials are independent variables. $\Delta\mu_O$ could be chosen as one of these independent variables, to relate the results of our analysis with the environmental conditions; $\Delta\mu_B = \Delta\mu_{Fe}$ is used here as the second independent variable. Contrary, A_a, B_b, O_c, is unstable, if

$$a'\Delta\mu_A + b'\Delta\mu_B + c'\Delta\mu_O \le \Delta E_{f,A_{a'}B_{b'}O_{c'}}, \quad (6)$$

where the first term could be eliminated using Eq. (4). In this study, we analyse the stability of $SrFeO_{3-\delta}$ and its possible decomposition into simple Sr- and Fe oxides (SrO, SrO_2, FeO, Fe_3O_4, and Fe_2O_3), elemental Sr and Fe metals, and O_2 gas.

Table 1 Inequalities, defining the boundaries of stability regions for various phases of $SrFeO_{3-\delta}$.

	Stability conditions for:					
	$SrFeO_3$			$SrFeO_{2.875}$		
Bounds for chemical potentials deviations:	$\Delta\mu_{Sr} + \Delta\mu_{Fe} + 3\Delta\mu_O = E_{f,SrFeO_3}$			$\Delta\mu_{Sr} + \Delta\mu_{Fe} + 2.875\Delta\mu_O = E_{f,SrFeO_{2.875}}$		
Prevents precipitation (release) of:		ECP	All-e		ECP	All-e
O_2 gas	$\Delta\mu_O \le 0$			$\Delta\mu_O \le 0$		
Sr	$\Delta\mu_O \ge (E_{f,SrFeO_3} - \Delta\mu_{Fe})/3$			$\Delta\mu_O \ge 8(E_{f,SrFeO_{2.875}} - \Delta\mu_{Fe})/23$		
Fe	$\Delta\mu_{Fe} \le 0$			$\Delta\mu_{Fe} \le 0$		
SrO	$\Delta\mu_O \ge (E_{f,SrFeO_3} - E_{f,SrO} - \Delta\mu_{Fe})/2$			$\Delta\mu_O \ge 8(E_{f,SrFeO_{2.875}} - E_{f,SrO} - \Delta\mu_{Fe})/15$		
SrO_2	$\Delta\mu_O \ge E_{f,SrFeO_3} - E_{f,SrO_2} - \Delta\mu_{Fe}$			$\Delta\mu_O \ge 8(E_{f,SrFeO_{2.875}} - E_{f,SrO_2} - \Delta\mu_{Fe})/7$		
FeO	$\Delta\mu_O \le E_{f,FeO} - \Delta\mu_{Fe}$			$\Delta\mu_O \le E_{f,FeO} - \Delta\mu_{Fe}$		
Fe_3O_4	$\Delta\mu_O \le (E_{f,Fe_3O_4} - 3\Delta\mu_{Fe})/4$			$\Delta\mu_O \le (E_{f,Fe_3O_4} - 3\Delta\mu_{Fe})/4$		
Fe_2O_3	$\Delta\mu_O \le (E_{f,Fe_2O_3} - 2\Delta\mu_{Fe})/3$			$\Delta\mu_O \le (E_{f,Fe_2O_3} - 2\Delta\mu_{Fe})/3$		
$SrFeO_3$				$\Delta\mu_O \le 8(E_{f,SrFeO_3} - E_{f,SrFeO_{2.875}})$	0.927	1.682
$SrFeO_{2.875}$	$\Delta\mu_O \ge 8(E_{f,SrFeO_3} - E_{f,SrFeO_{2.875}})$	0.927	1.682	-		
$SrFeO_{2.75}$	$\Delta\mu_O \ge 4(E_{f,SrFeO_3} - E_{f,SrFeO_{2.75}})$	1.050	0.825	$\Delta\mu_O \ge 8(E_{f,SrFeO_{2.875}} - E_{f,SrFeO_{2.75}})$	1.172	-0.032
$SrFeO_{2.5}$	$\Delta\mu_O \ge 2(E_{f,SrFeO_3} - E_{f,SrFeO_{2.5}})$	0.817	0.588	$\Delta\mu_O \ge 8(E_{f,SrFeO_{2.875}} - E_{f,SrFeO_{2.5}})/3$	0.780	0.223
	$SrFeO_{2.75}$			$SrFeO_{2.5}$		

Bounds for chemical potentials deviations: Prevents precipitation (release) of:	$\Delta\mu_{Sr} + \Delta\mu_{Fe} + 2.75\Delta\mu_O = E_{f,SrFeO_{2.75}}$			$\Delta\mu_{Sr} + \Delta\mu_{Fe} + 2.5\Delta\mu_O = E_{f,SrFeO_{2.5}}$		
		ECP	All-e		ECP	All-e
O_2 gas	$\Delta\mu_O \leq 0$			$\Delta\mu_O \leq 0$		
Sr	$\Delta\mu_O \geq 4(E_{f,SrFeO_{2.75}} - \Delta\mu_{Fe})/11$			$\Delta\mu_O \geq 2(E_{f,SrFeO_{2.5}} - \Delta\mu_{Fe})/5$		
Fe	$\Delta\mu_{Fe} \leq 0$			$\Delta\mu_{Fe} \leq 0$		
SrO	$\Delta\mu_O \geq 4(E_{f,SrFeO_{2.75}} - E_{f,SrO} - \Delta\mu_{Fe})/7$			$\Delta\mu_O \geq 2(E_{f,SrFeO_{2.5}} - E_{f,SrO} - \Delta\mu_{Fe})/3$		
SrO_2	$\Delta\mu_O \geq 4(E_{f,SrFeO_{2.75}} - E_{f,SrO_2} - \Delta\mu_{Fe})/3$			$\Delta\mu_O \geq 2(E_{f,SrFeO_{2.5}} - E_{f,SrO_2} - \Delta\mu_{Fe})$		
FeO	$\Delta\mu_O \leq E_{f,FeO} - \Delta\mu_{Fe}$			$\Delta\mu_O \leq E_{f,FeO} - \Delta\mu_{Fe}$		
Fe_3O_4	$\Delta\mu_O \leq (E_{f,Fe_3O_4} - 3\Delta\mu_{Fe})/4$			$\Delta\mu_O \leq (E_{f,Fe_3O_4} - 3\Delta\mu_{Fe})/4$		
Fe_2O_3	$\Delta\mu_O \leq (E_{f,Fe_2O_3} - 2\Delta\mu_{Fe})/3$			$\Delta\mu_O \leq (E_{f,Fe_2O_3} - 2\Delta\mu_{Fe})/3$		
$SrFeO_3$	$\Delta\mu_O \leq 4(E_{f,SrFeO_3} - E_{f,SrFeO_{2.75}})$	1.050	0.825	$\Delta\mu_O \leq 2(E_{f,SrFeO_3} - E_{f,SrFeO_{2.5}})$	0.817	0.588
$SrFeO_{2.875}$	$\Delta\mu_O \leq 8(E_{f,SrFeO_{2.875}} - E_{f,SrFeO_{2.75}})$	1.172	-0.032	$\Delta\mu_O \leq 8(E_{f,SrFeO_{2.875}} - E_{f,SrFeO_{2.5}})/3$	0.780	0.223
$SrFeO_{2.75}$	-			$\Delta\mu_O \leq 4(E_{f,SrFeO_{2.75}} - E_{f,SrFeO_{2.5}})$	0.584	0.350
$SrFeO_{2.5}$	$\Delta\mu_O \geq 4(E_{f,SrFeO_{2.75}} - E_{f,SrFeO_{2.5}})$	0.584	0.350			

Relevant expressions for boundaries of stability regions for target materials derived from Eqs. (4) and (6) for all considered compounds are collected in Table 1.

Molecules and non-metallic compounds usually are well described by hDFs. However, the description of metals is not so reliable. Additional problems appear, when the LCAO approximation is employed. These problems arise because calculations of metals demand the use of quite diffuse basis functions which are often difficult to optimize in metals. Besides, different calculations could be compared only, if they are performed using the same basis sets. To avoid explicit computations of metals and related complications, the total energy of an atom in a metal can be estimated using experimental values of the energy of formation for its oxide.[26] This estimate can be done using the definition of the Gibbs energies of formation for the binary oxides M_xO_y [48,50] :

$$E_M = \frac{1}{x}\left(E_{M_xO_y} - \Delta G^0_{f,M_xO_y} - \frac{y}{2}\left(E_{O_2} + \Delta G^{gas}_{O_2}(T^0, p^0) + \delta\mu^0_O\right)\right), \quad (7)$$

where $\Delta G^0_{f,M_xO_y}$ is the Gibbs energy of formation for M_xO_y under the standard conditions available from thermodynamic tables;[48,51] $E_{M_xO_y}$ the total energy of M_xO_y (per unit cell) and

Table 2 Lattice parameters and relative energy differences (ΔE) of $SrFeO_3$ phases

Description	Phase: Magnetic order	Space group: label	Space group: #	Obtained from	Basis set[a]	Lattice parameters: a=b, Å	c, Å	α=β, °	γ, °	Z[b]	ΔE, meV/f.u.
Cubic perovskite	FM	$Pm\bar{3}m$	221	Exptl.[52]		7.702	7.702	90	90	8	
Cubic perovskite	FM	$Pm\bar{3}m$	221	Opt./DFT+U [19]	PW	7.76	7.76	90	90	8	0
Cubic perovskite	AFM:G	$Pm\bar{3}m$	221	Opt./DFT+U [19]	PW	7.78	7.78	90	90	8	260
Cubic perovskite	FM	$Pm\bar{3}m$	221	Opt.	ECP	7.713	7.713	90	90	8	0
				Opt.	all-e	7.714	7.714	90	90	8	0
Distorted cubic perovskite	AFM:A	$P4mm$	99	Opt.	ECP	7.716	7.705	90	90	8	66
				Opt.	all-e	7.718	7.704	90	90	8	56
	AFM:C	$Cmmm$	65	Opt.	ECP	7.748	7. 736	90	89.99	8	172
				Opt.	all-e	7.776	7.736	90	89.78	8	148
	AFM:G	$R3m$	160	Opt.	ECP	7.768	7.768	89.47	89.47	8	393
				Opt.	all-e	7.773	7.773	89.64	89.64	8	414

[a] The computations with the ECP and all-electron (all-e) basis sets on Fe ion were performed. PW stands for plane wave basis set. [b] Z is the number of formula units in unit cell.

$\Delta G^{gas}_{O_2}(T^0, p^0)$ change of the Gibbs energy of oxygen gas from 0 *K* to the standard conditions.

Often several oxides for a given metal exist. In the case of SFO, two stable oxides (SrO and SrO_2) exists for Sr metal and three different oxides (FeO, Fe_2O_3, Fe_3O_4) are known for Fe. Thus, the metal energies here were obtained from several different oxides (e.g. for Fe atom from three oxides) are then averaged, to establish a common reference.

The *Gibbs energy of formation* for compound $A_aB_bO_c$

$$\Delta G_{f,A_aB_bO_c}(T,p_{O_2}) = E_{A_aB_bO_c} - aE_A - bE_B - c\mu_O(T,p_{O_2}) \quad (8)$$

can be re-written using the definitions for the variation of the O atom chemical potential (2) and the energy of formation (5) as

$$\Delta G_{f,A_aB_bO_c}(T,p_{O_2}) = \Delta E_{f,A_aB_bO_c} - c\Delta\mu_O(T,p_{O_2}), \quad (9)$$

This expression shows that, within our approximations, the dependence of Gibbs energy of formation on environmental conditions (temperature and oxygen partial pressure) arises entirely from the last term in Eq. 9. This expression illustrates also meaning of the energies of formation Eq. (5) as the Gibbs energies of formation at T=0*K*.

3. Results and discussion

Structure and relative energies for various related materials

To construct the phase diagrams, we began from calculations of very basic properties of relevant materials, such as the equilibrium atomic structure and the total energies (per formula unit) for considered phases of SFO, Sr and Fe oxides. The employed B3PW hybrid functional gives for the free O_2 molecule (used in our calculations as the reference state) the bond length of 1.202 Å and the bond energy of 5.38 eV, which agree well with the experimental values of 1.208 Å and 5.12 eV.[49] Computations of iron oxides were performed in our previous studies[22,23] under identical computational conditions as in the present study. Therefore, we used these results for FeO, Fe_3O_4, and Fe_2O_3 in the present study.

The results of lattice structure optimization for $SrFeO_3$ in all magnetic states are collected in Table 2. The FM state is found to be the lowest in energy, in agreement with experimental data[9] and plane-wave DFT+U calculations.[19] The order of different AFM states is the same for both basis sets on Fe ions: AFM:A state has the next lowest energy, followed by AFM:C, and AFM:G state has the highest energy within this group. The energy difference between AFM:G and FM states is reproduced reasonably well in calculations with ECP on Fe ions, in comparison with the calculations with full all-electron basis set at Fe: the underestimate is only 5%. However, such energy differences for AFM:A and AFM:C are overestimated by 18% and 16%. Optimization of the lattice constant for both basis sets on Fe produced the values of the constant (7.713 Å with ECP/ 7.714 Å all-electron) in much better agreement with the experimental value of 7.702 Å,[52] than DFT+U calculations.[19] The FM state is conductive, which is consistent with both experiment[9,14] and DFT+U calculations.[19]

Table 3 contains the results of lattice optimizations for $SrFeO_{2.875}$, where, in comparison to $SrFeO_3$, one oxygen atom per 8 formula units is removed in such a way to reproduce bulk-centered tetragonal structure presented at Fig. 2. The ground state for this crystal composition remains FM and conductive, in agreement with both experiment[9] and calculations.[19] The energy differences between FM and AFM states computed with ECP at Fe are significantly underestimated relatively to calculations with all-electron case. Such an underestimate for AFM:A and AFM:C is larger than 100 meV (per formula unit), and about half of that for AFM:G state. This leads for the energy difference between AFM-A and FM states calculated with ECP to be about a half of the same difference obtained from

Table 3 Lattice parameters and relative energy differences(ΔE) for $SrFeO_{2.875}$ phases

Description	Phase: Magnetic order	Space group: label	Space group: #	Obtained from	Basis set[a]	Lattice parameters: a=b, Å	Lattice parameters: c, Å	Z[b]	ΔE, meV/f.u.
Tetragonal bulk-centred	FM(helical)	$I4/mmm$	139	Exptl.[9]		10.900	7.684	16	
Tetragonal bulk-centred	FM	$I4/mmm$	139	Opt./DFT+U [19]	PW	11.03	7.76	16	0
	AFM:G			Opt./DFT+U [19]	PW	11.04	7.78	16	80
Tetragonal bulk-centred	FM	$I4/mmm$	139	Opt.	ECP	10.961	7.734	16	0
				Opt.	all-e	10.957	7.748	16	0
	AFM:A			Opt.	ECP	11.005	7.673	16	125
				Opt.	all-e	11.002	7.675	16	244
	AFM:C			Opt.	ECP	10.975	7.681	16	7
				Opt.	all-e	10.980	7.679	16	124
	AFM:G			Opt.	ECP	10.920	7.798	16	135
				Opt.	all-e	10.918	7.865	16	188

[a] The computations with the ECP and all-electron (all-e) basis sets on Fe ion were performed. PW stands for plane wave basis set. [b] Z is the number of formula units in unit cell.

Table 4 Lattice parameters and relative energy differences (ΔE) for $SrFeO_{2.75}$ phases

Description	Phase: Magnetic order	Space group: label	Space group: #	Obtained from	Basis set[a]	Lattice parameters: a, Å	b, Å	c, Å	Z[b]	ΔE, meV/f.u.
orthorhombic	AFM	$Cmmm$	65	Exptl.[9]		7.70	10.97	5.467	8	
orthorhombic	FM	$Cmmm$	65	Opt./DFT+U [19]	PW	7.78	11.09	5.52	8	100
	AFM:G			Opt./DFT+U [19]	PW	7.80	11.05	5.51	8	0
orthorhombic	FM	$Cmmm$	65	Opt.	ECP	7.770	11.005	5.491	8	119
				Opt.	all-e	7.784	11.007	5.490	8	136
	AFM:A(b)			Opt.	ECP	7.690	11.061	5.509	8	212
				Opt.	all-e	7.688	11.067	5.512	8	215
	AFM:C(b)			Opt.	ECP	7.724	11.010	5.494	8	0
				Opt.	all-e	7.732	11.013	5.496	8	0
	AFM:G			Opt.	ECP	7.766	10.986	5.479	8	35
				Opt.	all-e	7.776	10.984	5.477	8	22

[a] The computations with the ECP and all-electron (all-e) basis sets on Fe ion were performed. PW stands for plane wave basis set. [b] Z is the number of formula units in unit cell.

all-electron calculations. For AFM:C state such an underestimate is even more significant, since in calculations with all-electron description of Fe AFM:C state is located by 124 meV above the FM state. The calculations with ECP at Fe allocate the AFM:C state only by 7 meV above FM state. The optimized lattice constants are larger than experimental values less than 1%. This is a very good agreement, which was not achieved by DFT+U calculations.[19]

The results of calculations for $SrFeO_{2.75}$ are summarized in Table 4. The ground state of $SrFeO_{2.75}$ is AFM:C. Note that our consideration of magnetic state of $SrFeO_{2.75}$ was limited to a few spin configurations and was not capable reproducing details of the complicated magnetic ordering in this material.[12] In the present modelling, DFT+U calculations,[19] and in experiment[9] the ground state is insulating. The energy differences between ground AFM-C and all other magnetic states are in a reasonable agreement among calculations performed with ECP and the those using all-electron description. The obtained lattice structure for $SrFeO_{2.75}$ is also in very good agreement with the experimental one. Indeed, the calculated lattice constants overestimate experimental ones by less than 0.3% and, again, and are closer to the experimental results than achieved by the DFT+U computations.[19]

Lastly, $SrFeO_{2.5}$ has a brownmillerite structure (Fig. 4). To derive it from the cubic perovskite lattice, one has to remove one sixth of oxygen atoms from chains running along one of the [110] directions. Such chains of oxygen vacancies occur in each second octahedral layer. The resulting lattice has a layered structure, where layers of FeO_6 octahedra alternate with layers of FeO_4 tetrahedra. If rotations of tetrahedra are not allowed, such lattice has $Imma$ symmetry. Since tetrahedra are connected by corners, they can rotate only synchronously through each chain. Such rotations of tetrahedra produce an energy gain in $SrFeO_{2.5}$. In Fig. 4b-d red and blue shadings of tetrahedra mark opposite directions of their rotations. Three basic patterns (and corresponding phases) of tetrahedra rotations were considered: (i) tetrahedra within all chains rotate in the same direction – SG $Ibm2$, # 46; (ii) tetrahedra within chains of each layer rotate the same way, but with opposite rotation directions in neighboring layers – SG $Pbma$, # 57; (iii) alternation of rotation direction occurs already within each layer of tetrahedra - SG $Pnma$, # 62.

The results of optimization of above described brownmillerite lattices are assembled in Table 5. For all four primary structures for $SrFeO_{2.5}$, the lowest energy states have the AFM:G magnetic ordering. The high symmetry $Imma$ structure (Fig. 4a) has the largest energy (per formula unit) among considered phases. The structure with symmetry $Pbma$ appears to be the ground state. However, all three lower symmetry states have energies within a very few meV each from another. This variance is too small to reliably determine, which of these three states should be visible in experiment. The lattice structures of $SrFeO_{2.5}$ obtained from neutron diffraction experiments have been interpreted as $Imma$ [52,53] $Ibm2$,[54] or $Pbma$.[28,29] Evidently, it is not reliably settled. The obtained close energies for different structures predict that simultaneously several phases could coexist in the $SrFeO_{2.5}$ crystal and it is difficult to discern them in experiment. In such a case the high symmetry $Imma$ structure could be obtained due to averaging the diffraction picture over multiple

Table 5 Lattice parameters and relative energy differences (ΔE) of $SrFeO_{2.5}$ phases

Phase: Space group: label	Space group: #	Magnetic order	Obtained from	Basis set[a]	Lattice parameters: a, Å	b, Å	c, Å	Z[b]	ΔE, meV/f.u.
$Imma$	74	AFM:G	Exptl. [53]		5.6688	15.5775	5.5253	8	

$Imma$	74	AFM:G	Exptl. [52]		5.672	15.59	5.527	8	
$Ibm2$	46	AFM:G	Exptl. [54]		5.6685	15.5823	5.5265	8	
$Pbma$	57	AFM:G	Exptl. [29]		11.3505	15.5888	5.5288	16	
$Pbma$	57	AFM:G	Opt./DFT+U [55]	PW	11.311	15.407	5.503	16	0
$Ibm2$	46	AFM:G	Opt./DFT+U [55]	PW	5.659	15.402	5.501	8	13
$Pnma$	62	AFM:G	Opt./DFT+U [55]	PW	5.659	15.413	5.499	8	23
$Ibm2$	46	AFM:G	Opt./DFT+U [19]	PW	5.74	15.62	5.57	8	0
$Ibm2$	46	FM	Opt./DFT+U [19]	PW	5.77	15.70	5.58	8	270
$Imma$	74	FM	Opt.	ECP	5.763	15.213	5.669	8	418
		FM	Opt.	all-e	5.769	15.210	5.675	8	448
		AFM:A	Opt.	ECP	5.766	15.108	5.683	8	342
		AFM:A	Opt.	all-e	5.772	15.097	5.690	8	361
		AFM:C	Opt.	ECP	5.735	15.276	5.633	8	227
		AFM:C	Opt.	all-e	5.740	15.280	5.635	8	234
		AFM:G	Opt.	ECP	5.743	15.171	5.647	8	164
		AFM:G	Opt.	all-e	5.748	15.167	5.650	8	163
$Ibm2$	46	FM	Opt.	ECP	5.753	15.558	5.562	8	212
		FM	Opt.	all-e	5.764	15.541	5.569	8	242
		AFM:A	Opt.	ECP	5.762	15.453	5.573	8	138
		AFM:A	Opt.	all-e	5.773	15.424	5.583	8	158
		AFM:C	Opt.	ECP	5.723	15.599	5.542	8	64
		AFM:C	Opt.	all-e	5.724	15.649	5.545	8	73
		AFM:G	Opt.	ECP	5.736	15.489	5.556	8	1
		AFM:G	Opt.	all-e	5.744	15.468	5.562	8	1
$Pbma$	57	FM	Opt.	ECP	11.495	15.572	5.563	16	212
		FM	Opt.	all-e	11.519	15.549	5.570	16	242
		AFM:A	Opt.	ECP	11.511	15.463	5.576	16	138
		AFM:A	Opt.	all-e	11.534	15.436	5.585	16	158
		AFM:C	Opt.	ECP	11.439	15.608	5.544	16	63
		AFM:C	Opt.	all-e	11.455	15.595	5.549	16	73
		AFM:G	Opt.	ECP	11.462	15.501	5.558	16	0
		AFM:G	Opt.	all-e	11.480	15.476	5.564	16	0
$Pnma$	62	FM	Opt.	ECP	5.750	15.578	5.559	8	214
		FM	Opt.	all-e	5.762	15.559	5.566	8	244
		AFM:A	Opt.	ECP	5.758	15. 473	5.572	8	141
		AFM:A	Opt.	all-e	5.769	15.448	5.580	8	161
		AFM:C	Opt.	ECP	5.722	15.612	5.540	8	65
		AFM:C	Opt.	all-e	5.731	15.597	5.545	8	74
		AFM:G	Opt.	ECP	5.733	15.507	5.554	8	3
		AFM:G	Opt.	all-e	5.741	15.485	5.560	8	2

[a] The computations with the ECP and all-electron (all-e) basis sets on Fe ion were performed. PW stands for plane wave basis set. [b] Z is the number of formula units in unit cell.

(a) (b)

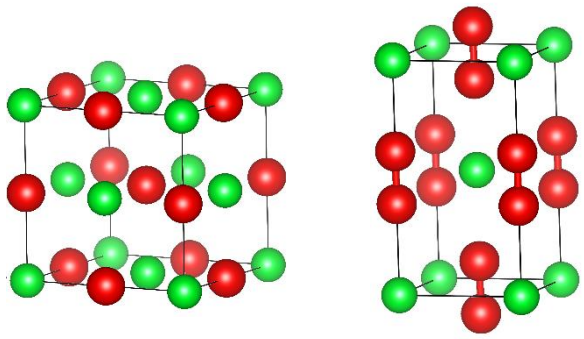

Fig. 5 Structures of strontium oxides (a) SrO, (b) SrO_2

Table 6 Lattice parameters of crystallographic cells for Sr oxides and z position of irreducible O atoms in SrO2 (in fractional coordinates)

Oxide	Obtained from	Phase	Symmetry group		Lattice parameters		z position of O atoms
			label	#	a=b, Å	c, Å	
SrO	Exptl.[57]	Rock salt, cubic	$Fm\bar{3}m$	225	5.16	5.16	
SrO_2	Exptl.[58]	Rock salt, cubic	$Fm\bar{3}m$	225	5.189	5.189	
		tetragonal	$I4/mmm$	139	3.563	6.616	0.388
		tetragonal	$I4/mmm$	139	3.557	6.776	0.391

crystallites, present in a sample. All calculated AFM:G states are non-conductive. Deviations of optimized lattice constants for $SrFeO_{2.5}$ are within 3% from the mentioned experimental

data, which is a sufficient agreement, considering the anisotropic crystal lattice of this material.

A comparison with the DFT+U calculations[19] shows usual larger overestimate than in the present work. Contrary, another DFT+U calculations[55] produced slightly underestimated set of lattice constants with respect to experiments. Note that the former calculations[19] considered only the $Ibm2$ structure of $SrFeO_{2.5}$, showing that energy of AFM:G state is smaller than the energy of the FM state, what is consistent with present results. Instead, comparison of the energies for all three low-symmetry structures of $SrFeO_{2.5}$ with AFM:G spin order in the DFT+U modelling, [55] points to the $Pbma$ structure as the ground state. This coincides with the present calculations, while the differences in the energies of these structures are by about an order of magnitude larger than in the present calculations. Note that these two DFT+U simulations were performed using different density functionals: PBE in ref. 19, and PBE with improved description of solids (PBEsol)[56] in ref. 55. In addition, the former calculations used Hubbard parameter *U*= 3 eV, while the latter one used *U*=5 eV. This could contribute to the difference in the results of two similar methods.

There are two known Sr oxides: SrO and SrO2, both are nonmagnetic. The former has a "rock salt" face-centered cubic structure (Fig. 5a). The lattice structure of SrO_2 is similar, but each O^{2-} ion is replaced by O_2^{2-}ion, oriented along one of the [001] directions; accordingly, the crystal is elongated in this direction. As the result, SrO_2 has a bulk-centered tetragonal lattice structure (Fig. 5b). The results of our crystalline structure optimization for Sr oxides are provided in Table 6. For SrO obtained lattice constant is in excellent agreement with experiment, exceeding it by less than 0.6%. The calculated unit cell for SrO_2 is more elongated than the experimental one. Its height exceeds that of the experimental cell by 2.5%, while lattice constants in other direction exceed the experimental ones only by less than 0.2%; all that indicates a good accuracy of calculations.

Table 7 The energies of formation (ΔEf) and standard Gibbs energies of formation (ΔG0f) of Sr and Fe oxides, and $SrFeO_{3-\delta}$

Material	Phase	Magnetic order	Basis set [a] or Expt.	ΔE_f, *eV* [b]	ΔG^0_f, *eV* [b]
FeO	cubic	AFM:[111]	Exptl.[51]	-2.88	-2.61
			ECP	-2.99	-2.71
			All-e	-3.05	-2.77
Fe_2O_3	α-phase	AFM	Exptl.[51]	-8.50	-7.68
			ECP	-8.38	-7.57
			All-e	-8.32	-7.45
Fe_3O_4	cubic	FiM: ↑↑ ↓↓↓↓[c]	Exptl.[51]	-11.63	-10.55
	rhombohedral		ECP	-11.48	-10.39
			All-e	-11.48	-10.39
SrO	rock salt		Exptl.[51]	-6.08	-5.81
			ECP	-6.27	-6.00
SrO_2	tetragonal		Exptl.[51]	-6.58	-6.03
			ECP	-6.39	-5.85
$SrFeO_3$	cubic	AFM:G	ECP/ECP	-10.61	-9.79
		AFM:G	All-e/ECP	-10.68	-9.87
$SrFeO_{2.875}$	tetragonal bulk-centered	FM	ECP/ECP	-10.72	-9.94
		FM	All-e/ECP	-10.89	-10.11
$SrFeO_{2.75}$	orthorhombic	AFM:C(b)	ECP/ECP	-10.87	-10.12
			All-e/ECP	-10.89	-10.14
$SrFeO_{2.5}$	brownmillerite	AFM:G	Expt.[18]	-11.04	-10.36 (-0.67; -0.49[17])
		AFM:G	ECP	-11.01	-10.33 (-0.56)
		AFM:G	All-e	-10.97	-10.29 (-0.58)

[a] The computations with the ECP and all-electron (all-e) basis sets on Fe ion were performed. Sr atoms are described with ECP only. [b] Values for $SrFeO_{2.5}$ in brackets are Gibbs energies of formation with respect to formation of the brownmillerite from oxides (SrO and Fe_2O_3). [c] The arrows denote the ferrimagnetic order in Fe_3O_4 with spins of four Fe ions in octahedral sites directed in opposite direction with respect to the spins of two Fe ions in tetrahedral sites of spinel lattice.[23]

Thermodynamic stability regions

The energy of a Fe atom in Fe metal and the energy of an O atom in an oxygen molecule were calculated in previous modelling.[22,23] Here we used the results for their energies as well as for the energies for iron oxide formation from these works. The energy of Sr atom in the metal was calculated using

Physical Chemistry Chemical Physics

ARTICLE

(a) ECP on Fe:

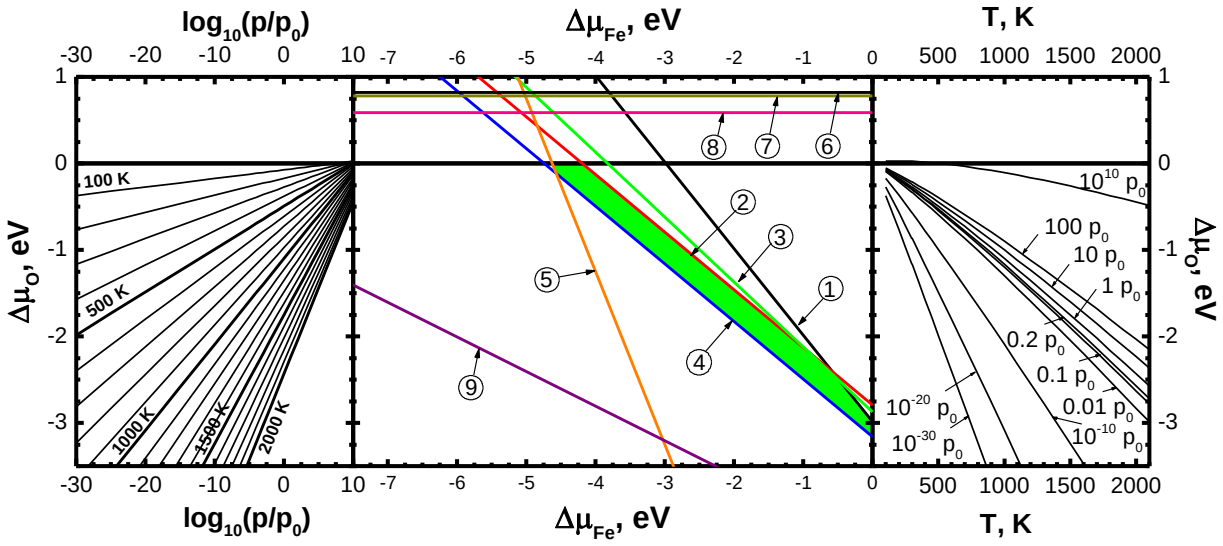

(b) All-electron Fe:

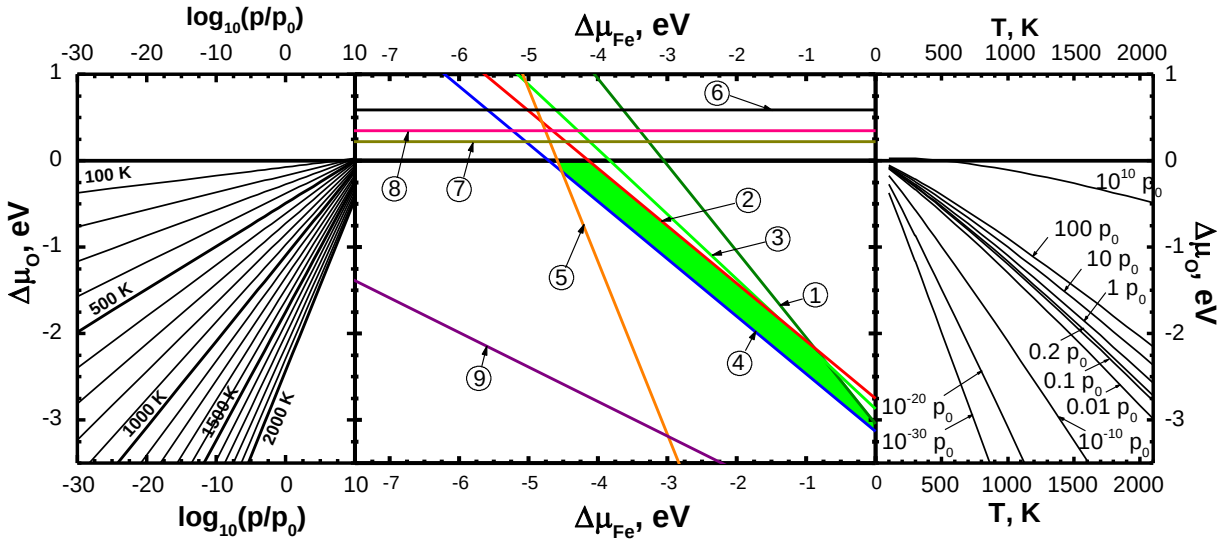

(c) Experimental:

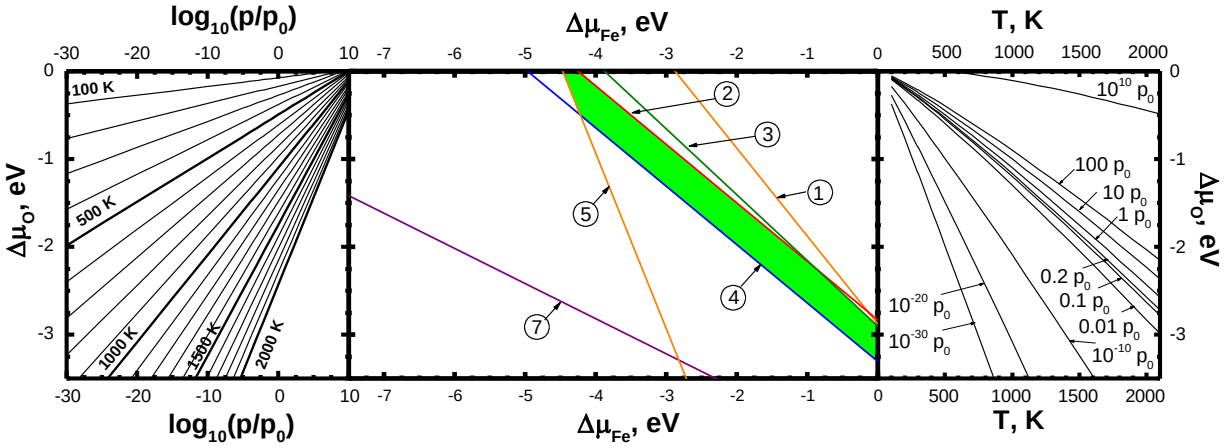

Fig. 6 Phase diagrams for $SrFeO_{2.5}$: (a) based on Fe ECP treatment (b) based on Fe all electron treatment (c) based on experimental energies of formation. The energies of formation used to build these diagrams are provided in Tables 1 and 7. The lines, pointed by numbers in circles describe conditions of forming of: (1) FeO, (2) Fe_2O_3, (3) Fe_3O_4, (4) SrO, (5) SrO_2, (6) $SrFeO_3$, (7) $SrFeO_{2.875}$, (8) $SrFeO_{2.75}$, (9) Sr metal. Green area marks $SrFeO_{2.5}$ stability region. Side panels at (a-c) serve to convert values of oxygen chemical potential $\Delta\mu_O$ to easy observable values of T and oxygen partial pressure p_{O_2} . This figure as well as all phase diagrams presented in following Figures are prepared using OriginPro 2015 package.[59]

Eq. (7) and then averaged over values derived from SrO and SrO_2 oxides. Using these energies, we re-calculated the formation energies for Sr oxides with respect to Sr in the metal. The obtained energies allow us calculations of the energies of formation (Eq. 5) and the standard Gibbs energies of formation (Eq. 8,9) for all four SFO phases. The results of calculations are summarized in Table 7. Here we do not discuss iron oxides, since they were treated earlier.[22,23]

The 3% error occurring in the final Gibbs energies of formation for strontium oxides rises due to averaging of Sr atom energy in metal phase obtained from two different Sr oxides. Comparison of the Gibbs energy of formation for SFO phases with experiment is possible only for $SrFeO_{2.5}$. The energies and the standard Gibbs energies of formation from elements for this composition are in excellent agreement with electrochemical measurements.[18] Accuracy of the Gibbs energy of formation from oxides is lower. This discrepancy (still within 15%) arises due to a less accurate reproduction of Gibbs energies of formation for oxides. High-temperature drop solution calorimetry experiments[17] provides the enthalpy of formation from oxides. To convert this to the Gibbs energy of formation, we extracted standard entropy for $SrFeO_{2.5}$ from electrochemical experiment[18] and used data for oxides from thermodynamic tables,[49] to calculate standard entropy of formation of $SrFeO_{2.5}$ from the oxides; the latter was combined with the enthalpy of formation from measurements[17] to produce respective experimental estimates for the Gibbs energy of formation of the brownmillerite phase from the oxides. The calculated energies lie between two mentioned experimental estimates for Gibbs energy of formation from oxides.

In the calculations, which used ECP on Fe atoms, the energy gain for perovskite formation from elements (per formula unit) monotonically increases with decreased oxygen content, i.e. from $SrFeO_3$ to $SrFeO_{2.5}$, suggesting enhanced stability. In all-electron calculations, $SrFeO_3$ appears still to be the least stable and $SrFeO_{2.5}$ is the most stable composition, while $SrFeO_{2.875}$ and $SrFeO_{2.75}$ compositions have very close energies.

The sequence of the formation energies of phases with different oxygen content (from $SrFeO_3$ to $SrFeO_{2.875}$, then to $SrFeO_{2.75}$, and finally to $SrFeO_{2.5}$) determine their relative stabilities. To illustrate this, we calculated the right-hand side of inequalities in the last four rows for each phase in Table 1, which describe stability conditions for different phases. (In these calculations the standard Gibbs energies of formation from Table 7 were used.) A positive $\Delta\mu_O$, corresponding to consequent transitions between these phases, immediately point to instability with respect to oxygen gas release. As the result the only stable phase is brownmillerite $SrFeO_{2.5}$, which is the last in the row. The values in the last lines of Table 1, have also the meaning of an average energy gain due to oxygen release. Taken with opposite sign, this is the energy of an oxygen vacancy formation. Correspondingly, the Gibbs energies calculated here for vacancies formation are negative for all three mentioned phases. At a first glance, such the result contradicts to the modelling,[19] where the energies of single oxygen vacancy formation have been found positive for all four SFO phases discussed here. In other words, formation of oxygen vacancies in simulations[19] cost energy, while in the present simulations it leads to an energy gain. This seeming contradiction can be reconciled by noticing that in ref. 19 a *single* vacancy is created in large supercells for each of SFO phases; therefore, interaction between the vacancies was largely avoided. Contrary, in our calculations phase transformations are associated with a high concentration of closely neighboring vacancies accompanying series of SFO transformations. Therefore, their mutual attraction could effectively lead to the negative average energies of vacancy formation.

Since the three first phases turned out to be thermodynamically unstable and the only stable phase left (within present model) is $SrFeO_{2.5}$, only this phase diagram is

presented in Fig. 6. Figs. 6a and 6b were constructed for both representations of Fe atoms: with ECP and with all-electron description. (The phase diagrams for three other phases could be found in ESI (Figures S1-S3)). The phase diagram for $SrFeO_{2.5}$ can also be constructed using the experimental data on the Gibbs formation energies for iron- and strontium oxides from thermodynamic tables[49] and for $SrFeO_{2.5}$ from electrochemical measurements,[18] while data on other phases of SFO are not required due to their instability. Such the diagram is plotted in

Fig. 6c. Side panels in all presented phase diagrams allow one to relate the oxygen chemical potential $\Delta\mu_O$ to observables: oxygen partial pressure and temperature.[23] More details on how to work with diagrams like the ones presented in Fig. 6 can be found in our previous paper.[23]

Because we restricted our SFO consideration to the phases with equal number of Sr and Fe atoms, the phase diagram does not contain any Sr-rich and Fe-reach materials. Within the employed approximation, no defects in crystals are allowed. The stability region of $SrFeO_{2.5}$ (marked in green in Fig. 6) is limited on above by condition $\Delta\mu_O < 0$, violation of which means release of oxygen gas.

Fig.6 allows us also to draw some conclusions on stabilities of SFO in the case of different Sr/Fe ratios. For instance, if Fe atoms are in slight excess, then $SrFeO_{2.5}$ should co-exist iron-rich double oxides (e.g. $SrFe_{12}O_{19}$, $SrFe_2O_4$, $Sr_4Fe_6O_{13}$). However, due to neglect of these phases in our modelling, the phase diagram suggests co-existence of $SrFeO_{2.5}$ only with iron oxides. With decreasing the oxygen chemical potential $\Delta\mu_O$ the excessive iron ions will be reduced and Fe_2O_3 oxide will be replaced, first for Fe_3O_4, and then FeO. With further decrease of $\Delta\mu_O$ excessive irons will be completely reduced to metallic phase, which still for while co-exists with $SrFeO_{2.5}$. And finally, iron from $SrFeO_{2.5}$ itself will also be reduced to a metal, leaving behind only SrO and Fe and released oxygen gas. Instead, in the phase diagram based on experimental energies of formation, the step of FeO formation is skipped and Fe_3O_4 is directly reduced to a metallic iron.

Similarly, for slight Sr-excess, $SrFeO_{2.5}$ should co-exist with strontium-rich double oxides (e.g. $Sr_3Fe_2O_6$, Sr_2FeO_4, $Sr_3Fe_2O_7$), but due to their neglect in the present model our phase

(a) ECP, B3PW

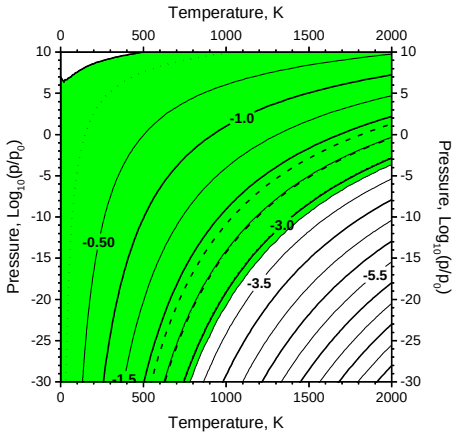

(b) all-electron, B3PW

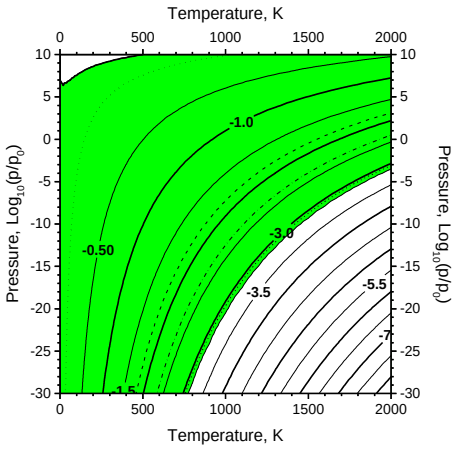

(c) Experimental data

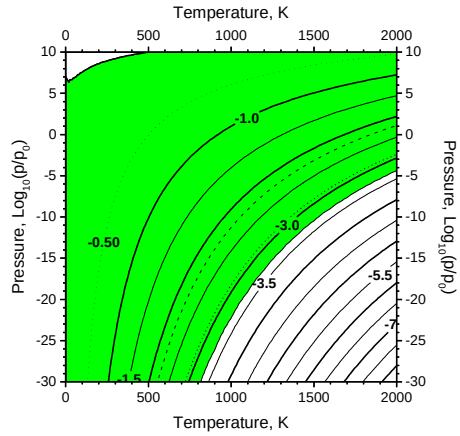

Fig. 7. Regions of SrFeO2.5 stability (green) vs temperature and oxygen pressure on the maps of oxygen chemical potential $\Delta\mu_O$ defined by Eq.(3). (a) The stability region for calculations with ECP at Fe ions; (b) The stability region for the Fe all-electron basis set; (c) The same with the experimental energies of formation. In this figure the short-dashed lines correspond to conditions, where an iron oxide (FeO in calculated diagram and Fe3O4 in the experimental one) coexists with metallic iron. These lines are very close to contour line at $\Delta\mu_O = 3\ eV$. The dashed lines correspond to coexisting Fe2O3 and Fe3O4. The dot-dash line represents conditions, where Fe3O4 coexists with FeO. The dot lines marks conditions, where SrO and SrO2 coexist. At plot (c) based on experimental data the later line coincides with contour line at $\Delta\mu_O = 0.5\ eV$. Corresponding reduction or oxidation occurs, when conditions cross these lines.

Table 8 Chemical potentials O atoms ($\Delta\mu_O$,eV) corresponding to crossings of precipitation lines and significant for the present analysis

Crossings between precipitation lines		$\Delta\mu_O, eV$		
		Exptl.	All-e at Fe	ECP at Fe
Fe_2O_3	Fe_3O_4	-2.22	-1.82	-2.18
Fe_3O_4	FeO		-2.34	-2.52
Fe_3O_4	Fe($\Delta\mu_{Fe} = 0\ eV$)	-2.91		
FeO	Fe($\Delta\mu_{Fe} = 0\ eV$)		-3.05	-2.99
SrO_2	SrO	-0.50	-0.12	-0.12
SrO	Fe($\Delta\mu_{Fe} = 0\ eV$)	-3.31	-3.14	-3.16

diagrams suggest formation of strontium oxides co-existing with $SrFeO_{2.5}$. Under O-rich conditions (high oxygen chemical potential $\Delta\mu_O$), the excess Sr is present in SrO_2 form, which transforms into SrO while $\Delta\mu_O$ becomes smaller. Lastly, at the O-poor side of diagram (a very low oxygen chemical potential $\Delta\mu_O$) SrFeO2.5 fully decomposes to SrO, Fe metal and O2 gas.

Table 8 summarizes the oxygen chemical potentials ($\Delta\mu_O$) where transformation of Fe- and Sr oxides and decomposition of $SrFeO_{2.5}$ take place. These data allow us to draw the region of stability for $SrFeO_{2.5}$ at a contour map of the oxygen chemical potential $\Delta\mu_O$ as a function of the observable environmental parameters: temperature T and oxygen partial pressure p_{O_2}. The information on the boundaries of the stability region, in terms of directly measurable physical parameters (T, p_{O_2}) is seen in the phase diagram in Fig. 6. However, it is more convenient to redraw the stability map (for $SrFeO_{2.5}$ here) by presenting the oxygen chemical potential as an explicit function of two independent environmental conditions (T, p_{O_2}). Such maps – theoretical (for both Fe atom basis sets) and derived from experimental data – are shown in Fig. 7. Each contour line in Fig. 7 corresponds to a constant value of $\Delta\mu_O$, in an interval between 0 eV and –8 eV, with the increment of -0.5 eV. The lower boundary of the stability region for $SrFeO_{2.5}$ is defined by the oxygen chemical potential, where the material decomposes. The upper boundary of the $SrFeO_{2.5}$ stability is the line for $\Delta\mu_O = 0$ eV, where release of O_2 gas begins. Additional lines are drawn at $\Delta\mu_O$, values where Fe or Sr atom oxidation states change according to Table 8.

4. Conclusions

The atomic structures of nonstoichiometric $SrFeO_{3-\delta}$ (δ=0, 0.125, 0.25, 0.5) and strontium oxides (SrO, SrO_2), which are among possible simple products of $SrFeO_{3-\delta}$ decomposition, were optimized, and the total energies for these structures were calculated using the B3PW hybrid density functional. The obtained energies of different phases were compared. The calculated atomic structures for different phases of $SrFeO_{3-\delta}$ and Sr oxides are in good agreement with experiments. The ground states for $SrFeO_3$ and $SrFeO_{2.875}$ were found to be metallic and having FM spin ordering, in agreement with the experiment.[9] In contrast, the ground states of $SrFeO_{2.75}$ and $SrFeO_{2.5}$ are insulating. Spins in the ground state of $SrFeO_{2.5}$ are arranged according AFM:G ordering, also in agreement with experiment.[9]

The present calculations yield the Gibbs energies of formation for a series of $SrFeO_{3-\delta}$ (δ=0, 0.125, 0.25, 0.5) and strontium oxides (SrO, SrO_2). These energies were used to construct the phase diagrams and stability regions for all four considered SFO compositions. Only $SrFeO_{2.5}$ composition is predicted to be stable. An analogous diagram for $SrFeO_{2.5}$ was constructed using the experimental Gibbs energies of formation. These diagrams allow us to understand possible chemical transformations in the system, whenever the system contains equal numbers of Sr and Fe atoms or there is an excess of one of these metals. (The results of calculations for iron oxides (FeO, Fe_3O_4, and Fe_2O_3) were discussed in refs. 22, 23.)

Our hybrid B3PW calculations with optimized basis sets give $SrFeO_{2.5}$ energy of formation from binary oxides which is underestimated with respect to electrochemical measurements,[18] while it is larger, than the value derived from drop solution calorimetry.[17] At the same time, the standard Gibbs energy of formation from elements almost coincide with that from the experiments.[18] The larger error in Gibbs energy of formation of $SrFeO_{2.5}$ from oxides is related to inconsistency of the energy for atoms of Sr and Fe metals, when determined from different oxides.

The oxygen chemical potential range, in which $SrFeO_{2.5}$ is stable and co-exists with various oxides or metallic iron, were determined from the phase diagrams and drawn as contour maps. This allowed us to compare theoretical prediction of $SrFeO_{2.5}$ stability regions with the same regions obtained from the experimental data in terms of temperature and oxygen partial pressure, which can be directly obtained from measurements. Such contour maps are also much more convenient to use in experimental and industrial settings because they are drawn in terms of immediately accessible measurement results.

Comparison of the Gibbs energies of formation for different nonstoichiometric phases of $SrFeO_{3-\delta}$ indicates an increase in stability of phases with growing number of oxygen vacancies. The precipitation lines for these phases with non-stoichiometries δ=0, 0.125, 0.25 are located at positive oxygen chemical potentials. All these facts together with positive energies of formation of an additional single oxygen vacancy in $SrFeO_{3-\delta}$, obtained in earlier DFT+U simulations[19] suggest strong mutual attraction between the vacancies and spontaneous formation on vacancy clusters during a series of $SrFeO_3$ - $SrFeO_{2.875}$ - $SrFeO_{2.75}$ - $SrFeO_{2.5}$ transformations. The latter conclusion still requires direct confirmation by respective modelling and will strongly influence mechanisms of formation of different phases in SFO.

Conflicts of interest

There are no conflicts to declare.

Acknowledgements

Authors are greatly indebted to R. Merkle and J. Serra for many stimulating discussions and to J. Young for help with understanding brownmillerite structures. E.H. thanks also Department of Physical Chemistry of the Max Planck Institute for Solid State Research for long-term hospitality and support. E.H., A.B. and EK acknowledge also the Russian Science Foundation for provided partial financial support through funding under the project 14-43-00052 for the analysis of the experimental literature on complex perovskite formation enthalpies. The computer resources were provided by Stuttgart Supercomputing Centre (Project DEFTD 12939) and

the National Research Nuclear University MEPhI, Moscow, Russia.

References

1 M. Kuklja, E. Kotomin, R. Merkle, Y. Mastrikov and J. Maier, *Phys. Chem. Chem. Phys.*, 2013, **15**, 5443-5471.
2 B. Schmid, G. Rupp and J. Fleig, *Phys. Chem. Chem. Phys. ,* 2018, **20**, 12016-12026.
3 D. Gryaznov, R. Merkle, E. Kotomin and J. Maier, *J. Materials Chem. A,* 2016, **4**, 13093-13104.
4 D. Gryaznov, S. Baumann, E. Kotomin and R. Merkle, *J. Phys. Chem. C*, 2014, **118**, 29542-29553.
5 F. S. Baumann, J. Fleig, G. Cristiani, B. Stuhlhofer, H.-U. Habermeier and J. Maier, *J. Electrochem. Soc.*, 2007, **154**, B931-B941.
6 G. Dong, H. Fan, H. Tian, J. Fang and Q. Li, *RSC Adv.*, 2015, **5**, 29618–29623.
7 P. S. Maiya, U. Balachandran, J. T. Dusek, R. L. Mieville, M. S. Kleefisch and C. A. Udovich, *Solid State Ionics*, 1997, **99**, 1–7.
8 V. Celorrio, K. Bradley, O. J. Weber, S. R. Hall and D. J. Fermín, *ChemElectroChem*, 2014, **1**, 1667–1671.
9 M. Reehuis, C. Ulrich, A. Maljuk, C. Niedermayer, B. Ouladdiaf, A. Hoser, T. Hofmann and B. Keimer, *Phys. Rev. B: Condens. Matter Mater. Phys.,* 2012, **85**, 184109.
10 Y. Takeda, K. Kanno, T. Takada, O. Yamamoto, M. Takano, N. Nakayama and Y. Bando, *J. Solid State Chem.,* 1986, **63**, 237–249.
11 C. Haavik, T. Atake and S. Stolen, *Phys. Chem. Chem. Phys.*, 2002, **4**, 1082-1087.
12 M. Schmidt, M. Hofmann and S. J. Campbell, *J. Phys.: Condens. Matter*, 2003, **15**, 8691-8701.
13 K. Momma and F. Izumi, *J. Appl. Crystallogr*., 2011, **44**, 1272-1276.
14 S. Ishiwata, M. Tokunaga, Y. Kaneko, D. Okuyama, Y. Tokunaga, S. Wakimoto, K. Kakurai, T. Arima, Y. Taguchi and Y. Tokura, *Phys. Rev. B: Condens. Matter Mater. Phys.*, 2011, **84**, 054427.
15 A. Lebon, P. Adler, C. Bernhard, A. V. Boris, A. V. Pimenov, A. Maljuk, C. T. Lin, C. Ulrich and B. Keimer, *Phys. Rev. Lett.*, 2004, **92**, 037202.
16 P. Adler, A. Lebon, V. Damljanović, C. Ulrich, C. Bernhard, A. V. Boris, A. Maljuk, C. T. Lin and B. Keimer, *Phys. Rev. B: Condens. Matter Mater. Phys.*, 2006, **73**, 094451.
17 J. Cheng, A. Navrotsky, X.-D. Zhou and H. U. Anderson, *Chem. Mater.*, 2005, **17**, 2197-2207.
18 S. K. Rakshit, S. C. Parida, S. Dash, Z. Singh, B. K. Sen and V. Venugopal, *J. Solid State Chem*., 2007, **180**, 523–532.
19 T. Das, J. D. Nicholas and Y. Qi, *J. Mater. Chem. A,* 2017 **5**, 4493-4506.
20 J. P. Perdew, K. Burke and M. Ernzerhof, *Phys. Rev. Lett.,* 1996, **77**, 3865–3868.
21 S. L. Dudarev, G. A. Botton, S. Y. Savrasov, C. J. Humphreys and A. P. Sutton, *Phys. Rev. B: Condens. Matter Mater. Phys.*, 1998, 57, 1505-1509.
22 E. Heifets, E. A. Kotomin, J. Maier and A. A. Bagaturyants, *J. Phys. Chem. Lett.*, 2015, **6**, 2847−2851.
23 E. Heifets, E. A. Kotomin, A. A. Bagaturyants and J. Maier, *Phys.Chem.Chem.Phys.*, 2017, **19**, 3738-3755.
24 S. Piskunov, E. Heifets, R. I. Eglitis and G. Borstel, *Comput. Mater. Sci.,* 2004, **29**, 165–178.
25 E. Heifets, S. Piskunov, E. A. Kotomin, Y. F. Zhukovskii and D. E. Ellis, *Phys. Rev. B: Condens. Matter Mater. Phys.*, 2007, **75**, 115417.
26 E. A. Ahmad, L. Liborio, D. Kramer, G. Mallia, A. R. Kucernak and N. M. Harrison, *Phys. Rev. B: Condens. Matter Mater. Phys.: Condens. Matter Mater. Phys.*, 2011, 84, 085137.
27 R. Dovesi, V. R. Saunders, C. Roetti, R. Orlando, C. M. Zicovich-Wilson, F. Pascale, B. Civalleri, K. Doll, N. M. Harrison, I. J. Bush and et al., *CRYSTAL09 User's Manual*, University of Torino, Torino, 2009.
28 J. E. Auckett, A. J. Studer, E. Pellegrini, J. Ollivier, M. R. Johnson, H. Schober, W. Miiller and C. D. Ling, *Chem. Mater.* , 2013, **25**, 3080-3087.
29 J. E. Auckett, A. J. Studer, N. Sharma and C. D. Ling, *Solid State Ionics*, 2012, **225**, 432-436.
30 H. Monkhorst and J.D. Pack, *Phys. Rev. B: Condens. Matter Mater. Phys.* , 1976, **13**, 5188-5192.
31 A. D. Becke, *J. Chem. Phys.*, 1993, **98**, 5648-5652.
32 J. P. Perdew and Y. Wang, *Phys. Rev. B: Condens. Matter Mater. Phys.*, 1986, **33**, 8800-8802.
33 J. P. Perdew and Y. Wang, *Phys. Rev. B: Condens. Matter Mater. Phys.*, 1989, **40**, 3399.
34 J. P. Perdew, in *Electronic Structure of Solids*, ed. P. P. Ziesche and H. Eschrig, vol. 11, Akademie Verlag, Berlin, 1991, pp. 11-20.
35 P. A. M. Dirac, *Proc. Cambridge Phil. Soc.,* 1930, **26**, 376.
36 J. P. Perdew and Y. Wang, *Phys. Rev. B: Condens. Matter Mater. Phys.*, 1992, **45**, 13244.
37 E. Heifets, S. Piskunov, E. A. Kotomin, Y. F. Zhukovskii and D. E. Ellis, *Phys. Rev. B: Condens. Matter Mater. Phys.*, 2007, **75**, 155431.
38 Stuttgart/Cologne energy-consistent (ab initio) pseudopotentials, http://www.tc.uni-koeln.de/PP/index.en.html (Accessed June 2018).
39 Collection of basis sets optimized for calculations with CRYSTAL code, http://www.crystal.unito.it/basis-sets.php (Accessed June 2018).
40 I. Lim, H. Stoll and P. Schwerdtfeger, *J. Chem. Phys.*, 2006, **124**, 034107.
41 ECP for Sr, http://www.tc.uni-koeln.de/cgi-bin/pp.pl?language=en,format=crystal09,element=Sr,job=getecp,ecp=ECP28MDF (Accessed June 2018).
42 Basis set for Sr (Sr_ECP28MDF_s411p411d11_Heifets_2013), http://www.crystal.unito.it/Basis_Sets/strontium.html#Sr_ECP28MDF_s411p411d11_Heifets_2013 (Accessed June 2018).
43 Basis set for O (O_8411(d11)_Heifets_2013), http://www.crystal.unito.it/Basis_Sets/oxygen.html#O_8411(d11)_Heifets_2013 (Accessed June 2018).
44 M. Dolg, U. Wedig, H. Stoll and H. Preuss, *J. Chem. Phys.*, 1987, **86**, 866-872.
45 ECP for Fe, http://www.tc.uni-koeln.de/cgi-bin/pp.pl?language=en,format=crystal09,element=Fe,job=getecp,ecp=ECP10MDF (Accessed June 2018).
46 Basis set for Fe (Fe_ECP10MFD_s411p411d411_Heifets_2013), http://www.crystal.unito.it/Basis_Sets/iron.html#Fe_ECP10MFD_s411p411d411_Heifets_2013 (Accessed June 2018).
47 All-electron basis set for Fe (Fe_s86411p6411d411_Heifets_2013), http://www.crystal.unito.it/Basis_Sets/iron.html#Fe_s86411p6411d411_Heifets_2013 (Accessed June 2018).

48 K. Reuter and M. Scheffler, *Phys. Rev. B: Condens. Matter Mater. Phys.*, 2001, **65**, 035406.
49 P. J. Linstrom and W. G. Mallard, Eds., *NIST Chemistry WebBook, NIST Standard Reference Database*, vol. 69, National Institute of Standards and Technology, Gaithersburg, 2003.
50 K. Johnston, M. R. Castell, A. T. Paxton and M. W. Finnis, *Phys. Rev. B: Condens. Matter Mater. Phys.*, 2004, **70**, 085415.
51 L. f. T. Hüttenkunde, Ed., *Thermodynamic Properties of Inorganic Materials, Landolt-Börnstein, New Series, Group IV*, vol. 19, Springer,Berlin, 1999.
52 J. Hodges, C. Short, J. Jorgensen, X. Xiong, B. Dabrowski, S. Mini and C. Kimball, *J. Solid State Chem.*, 1999, **151**, 190-209.
53 P. Berastegui, S.-G. Eriksson and S. Hull, *Mater. Res. Bull.*, 1999, **34**, 303-314.
54 M. Schmidt and S. Campbell, *J.Solid State Chem.*, 1999, **156**, 292-304.
55 J. Young and J. M. Rondinelli, *Phys. Rev. B: Condens. Matter Mater. Phys.*, 2015, **92**, 174111.
56 J. P. Perdew, A. J. P.Ruzsinszky, G. I. Csonka, O. A. Vydrov, G. E. Scuseria, L. A. Constantin, X. Zhou and K. Burke, *Phys. Rev. Lett.*, 2008 , **100**, 136406.
57 D. Taylor, *Trans. British Ceram. Soc.* 1984, 83, 5.
58 M. Koenigstein, *J. Solid State Chem.*, 1999, **147**, 478-484.
59 OriginPro code, OriginLab, Northampton, MA https://www.originlab.com/# (Accessed June 2018).

Institute of Solid State Physics, University of Latvia as the Center of Excellence has received funding from the European Union's Horizon 2020 Framework Programme H2020-WIDESPREAD-01-2016-2017-TeamingPhase2 under grant agreement No. 739508, project CAMART²

